Physical and Numerical Experiment with Extreme Hydroelastic Wave Impacts at Scale

Bockstael, M.M.[1,2,*] and Wellens, P.R.[1,*]

[1] Ship Hydromechanics Laboratory, Delft University of Technology, Delft, Netherlands
[2] Maritime Research Institute Netherlands, Wageningen, Netherlands

Abstract. This study concerns repeatable wave impacts, including large variations of the interfaces and hydroelastic structural response, using physical and numerical tests at scale. The physical tests consist of a rectangular, oscillating tank that produces a sloshing wave impact against a flexible, overhanging, cantilever plate. The numerical setup consists of a hydrostructural model, where the hydrodynamic part is a two-phase finite-volume Navier-Stokes solver. The structural part is a finite-element discretisation of a beam, which is monolithically coupled to the fluid solver. Comparing physical and numerical results serves both the validation of the numerical model and the interpretation of the physical tests.

Key words: *Wave impact; Cantilever; Overhang; CFD; Monolithic coupling*

1. Introduction

Extreme wave impacts can exert high loads on maritime structures, which can lead to damage or failure. In literature, commonly mentioned categories of wave impact are slamming [1], sloshing [2] and green water [3]. The occurrence of the most extreme wave impacts is rare, which makes it hard to obtain converged statistics of extreme values [4, 5]. Controlled, artificially generated wave impacts are therefore important tools for the study of the expected value and variability of these events. The dynamics of extreme wave impacts involve large variations of the interfaces and response of the impacted structure, which are among the main sources of nonlinearities in slamming [6]. The hydrodynamic loads and structural response depend on their fluid-structure interaction, which should be taken into account as hydroelasticity during wave impacts [7, 8].

A recent review on flexible fluid-structure interactions in the ocean by [6] provides comprehensive lists of slamming studies and tests. The authors provide a history of the development of efficient and accurate semi-analytical models, but state their main limitation is in addressing more complex scenarios, such as those involving cavitation, air cushions and compressibility. For sloshing impacts these complex physical effects should be considered, but correct numerical modelling and scaling of the fluid-structure interactions is still beyond the state of the art [2]. Computational fluid dynamics (CFD) methods may address this complexity in the future, but challenges remain in developing efficient and appropriate methods for coupling the fluid and structural solvers [6]. Numerical methods, like CFD, do not require expensive physical setup and are less limited in configuration compared to analytical models. Additionally, the ability to define independent material properties is valuable for identifying scaling effects relevant to wave impacts [9]. Modelling these additional physical effects will require rigorous validation benchmarks.

This study concerns repeatable wave impacts using numerics and physical tests at scale. The experimental wave impact setup used in this study includes a free surface and a flexible structure, but differs

*Correspondence to: m.m.bockstael@tudelft.nl, p.r.wellens@tudelft.nl

from the more common wedge or plate drop tests. The tests consist of a rectangular, oscillating tank that produces a sloshing wave impact against a flexible, overhanging, cantilever plate. A numerical hydrodynamic model, specifically developed for extreme wave impacts, is coupled to a structural model of a cantilever beam. The hydrodynamic model consists of a two-phase finite-volume discretisation of the Navier-Stokes equations [10]. The structural model consists of a finite-element discretisation of the Euler-Bernoulli beam equation. The hydrostructural coupling is done using a monolithic approach to resolve the two-way interaction, and includes the geometric deformation of the beam. This allows the comparison between simulated and measured structural deflection, which is used to validate the numerical model. The combination of physical and numerical experiments increases confidence in the accuracy and interpretation of the results.

In section 2 the hydrostructural model is introduced. The physical experiment and its numerical reproduction are described in section 3. The validation of the numerical model is presented in section 4. Finally, section 5 discusses hydroelastic effects and is followed by concluding remarks.

2. Numerical model

2.1. Hydrodynamic model

The hydrodynamic model of [10] is adopted, which is based on the conservation equations for mass (Eq. 1) and momentum (Eq. 2) of the fluid. Viscous stresses are left out of the momentum equation, because their effect of is assumed negligible during the short duration of an impact.

$$\frac{\partial \rho}{\partial t} + \nabla \cdot \rho \vec{u} = 0 \tag{1}$$

$$\frac{\partial \left(\rho \vec{u}\right)}{\partial t} + \nabla \cdot \rho \vec{u}\vec{u}^T = -\nabla p + \rho g \tag{2}$$

Here ρ is the fluid density, $\vec{u}$ its velocity, p the pressure, and g the gravitational acceleration. In accordance with the Volume-of-Fluid method (VoF), Eq. 3 for colour function α is used to track the interface between air and water, where $\alpha = 0$ and 1, respectively.

$$\frac{\partial \alpha}{\partial t} + \nabla \cdot \alpha \vec{u} - \alpha \nabla \cdot \vec{u} = \frac{D\alpha}{Dt} = 0 \tag{3}$$

An aggregated fluid density can be defined by averaging over volume V as $\rho = |V|^{-1} \int_V \rho(\vec{x})\, dV$. By doing the same for α, both are related by Eq. 4 using constant (incompressible flow) densities of the two separate phases: water (ρ_1) and air (ρ_2).

$$\rho = \alpha\rho_1 + (1-\alpha)\rho_2 \tag{4}$$

Throughout the description of the aggregated fluid model, quantities refer to their volume-averaged values according to a finite-volume discretisation. A staggered arrangement of control volumes on the cartesian cell faces is adopted for velocities, whereas all other variables, such as density, colour function and pressure, are defined over control volumes that coincide with grid cells. The advection of the free surface via α in Eq. 3 is done using the symmetric, split (COSMIC) scheme in two dimensions [11, 12]. The interfaces are reconstructed as piecewise lines (PLIC) using the analytic relations by [13].

Extreme wave impacts involve large free surface deformations and loads depend mainly on the inertia of the fluid. To accurately model the free surface dynamics, consistency between mass and momentum transport on the staggered control volumes is required [14]. Therefore, an intermediate ($*$) step is used in the advection of momentum using Eq. 5, where intermediate density ρ^* is found by solving Eq. 6 on the staggered control volumes. Without this approach, the simulated wave impact differed significantly from the physical experiment.

$$\frac{\rho^* \vec{u}^* - \rho^n \vec{u}^n}{\delta t^{n+1}} + \nabla \cdot \rho^\alpha \vec{u}^n (\vec{u}^n)^T = 0 \tag{5}$$

$$\frac{\rho^* - \rho^n}{\delta t^{n+1}} + \nabla \cdot \rho^\alpha \vec{u}^n = 0 \tag{6}$$

Here ρ^α indicates that the mass fluxes are based on the transport of mass via α in Eq. 3. Advecting velocities are determined using the first-order upwind scheme, and the time integration scheme is forward Euler as shown in Eqs. 5 and 6. The time step $\delta t^{n+1} = t^{n+1} - t^n$ is adapted to satisfy criteria that guarantee numerical stability.

The rest of the solution strategy consists of the projection method, which results in a single Poisson equation that has to be solved. Eq. 2 is rewritten to the velocity update Eq. 7.

$$\frac{\vec{u}^{n+1} - \vec{u}^*}{\delta t^{n+1}} = -\frac{1}{\rho^{n+1}} \nabla p^{n+1} + g\,. \tag{7}$$

The Poisson Eq. 8 for the pressure update $\delta p^{n+1} = p^{n+1} - p^n$ is then obtained by substituting Eq. 7 into $\nabla \cdot \vec{u}^{n+1} = 0$.

$$\delta t^{n+1} \nabla \cdot \frac{1}{\rho^{n+1}} \nabla \delta p^{n+1} = \nabla \cdot \left(\vec{u}^* - \frac{\delta t^{n+1}}{\rho^{n+1}} \nabla p^n + \delta t^{n+1} g \right) \tag{8}$$

Eq. 8 can be written to the linear system in Eq. 9 with matrix A and vector r.

$$\delta t^{n+1} \mathrm{A}^n \, \delta p^{n+1} = r^n(\delta t^{n+1}) \tag{9}$$

2.2. Structural model and coupling

The flexible plate is modelled as a 1D dynamic Euler-Bernoulli beam, with governing equation

$$\mu \frac{\partial^2 w(t,s)}{\partial t^2} + EIw''''(t,s) = q(t,s) \tag{10}$$

where w is the deflection normal to length-coordinate s. The term EIw'''' is the constant bending stiffness multiplied by the fourth spatial derivative of the deflection. The remaining terms are constant mass per unit length μ and distributed load $q(t,s)$.

A finite-element (FE) discretisation with cubic Hermite elements is applied to Eq. 10. The same symbols w and q now represent discrete nodal values in the resulting system Eq. 11 of differential equations, with mass and stiffness matrices M and K, respectively.

$$\mathrm{M} \, \frac{\partial^2 w(t)}{\partial t^2} + \mathrm{K} \, w(t) = q(t) \tag{11}$$

The system of linear Eqs. 12 and 13 is obtained using backward Euler time discretisation, where the first time derivative $\dot{w}$ is introduced as an additional variable. Coupling matrix C_p is introduced to express variable load q^{n+1} in terms of piecewise-constant fluid pressures p.

$$\mathrm{M} \, \frac{\dot{w}^{n+1} - \dot{w}^n}{\delta t^{n+1}} + \mathrm{K} \, w^{n+1} \quad = \quad \mathrm{C}_p \, p^{n+1} \tag{12}$$

$$\frac{w^{n+1} - w^n}{\delta t^{n+1}} \quad = \quad \dot{w}^{n+1} \tag{13}$$

The monolithic hydrostructural coupled system Eq. 14 is then completed by the coupling matrix $\mathrm{C}_{\dot{w}}$ that relates $\dot{w}$ to fluid velocities $\vec{u}$.

$$\begin{bmatrix} \delta t^{n+1} \mathrm{A}^n & \mathrm{C}_{\dot{w}}^n & \\ \delta t^{n+1} \mathrm{C}_p^n & \mathrm{M} & \delta t^{n+1} \mathrm{K} \\ & \delta t^{n+1} \mathrm{I} & -\mathrm{I} \end{bmatrix} \begin{bmatrix} \delta p \\ \dot{w} \\ w \end{bmatrix}^{n+1} = \begin{bmatrix} r^n(\delta t^{n+1}) \\ \mathrm{M} \, \dot{w}^n - \delta t^{n+1} \mathrm{C}_p^n \, p^n \\ w^n \end{bmatrix} \tag{14}$$

During coupled hydrostructural simulation, the beam deformation is applied to the fluid domain using cut cells, as shown for example in Fig. 1. Cut cells define regions that are open to fluid flow using cell volume and face apertures. It is continuously ensured that there is a staircase-like sequence of fully closed fluid cell faces along the length of the beam. The minimum thickness of the beam representation in the fluid domain is thus related to the fluid cell height.

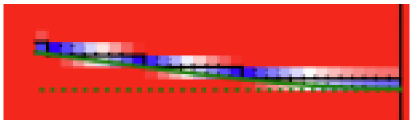

Figure 1: A visualisation of cut cells around a deformed beam. The continuous green curve shows the deformation of the beam compared to the dotted, zero deflection line. Fluid cell volume apertures are indicated by cell colours ranging from fully open (red) to closed (blue). Face apertures are shown by (dotted) black lines for (partly) closed faces.

3. Wave impact experiment

3.1. Physical setup

The physical experiment simulates wave impacts on a cantilever overhang by sloshing waves in a rectangular tank, with dimensions as drawn in Fig. 2a. From standstill, the tank is excited in horizontal oscillatory motion close to the natural frequency of the fluid. This generates fast run up of a fluid wedge along the wall that impacts the overhanging plate, as seen in Figs. 2b and 2c. The thinnest and thickest plates tested have thicknesses $d_t = 0.4$ and 4.0 mm, respectively.

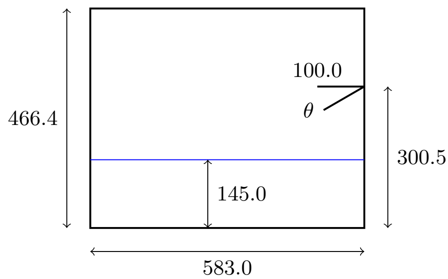

(a) Dimensions of the domain in millimetres. Depth of the fluid domain into the page is 200.0 mm. The plate has a clearance of 1.0 mm at both sides.

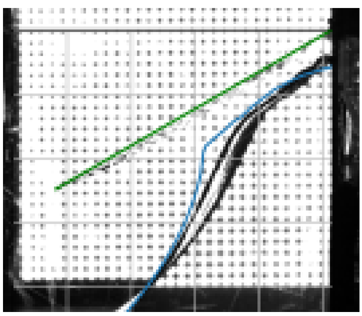

(b) Overlay of numerical simulation on video snapshot. Not exactly synchronised.

(c) Incoming wave impact on thick 4.0 mm plate instrumented with multiple, different pressure sensors. Zemic H3 50 kg reaction load cell at the top.

Figure 2: Experimental setup

The instrumentation of the measurement setup consists of reaction load cells and pressure sensors (Fig. 2c), and three laser distance sensors of type Panasonic HG-C1400 at different positions along the plate (not shown). Only the 4.0 mm plate was instrumented with pressure sensors, since it is so stiff that no significant deflection occurs. The thinner plate was not instrumented with pressure sensors, in order not to affect plate inertia. Strain gauges could give insight into plate stress, but were not used in this setup. The combination of total reaction load, pressure and deflection is considered enough data to validate the hydrostructural model.

3.2. Numerical reproduction

The physical experiment is numerically reproduced according to the dimensions in Fig. 2a. Gravitational acceleration is assumed $g = 9.81$ m s^{-2} and the only fluid properties are the densities of water $\rho_1 = 1000$ kg m^{-3} and air $\rho_2 = 1.2$ kg m^{-3}. Fluid viscosity and surface tension are not modelled. The bending moment of inertia I of the plate is determined from its width $d_w = 198.0$ mm and its thickness d_t. The assumed structural properties of the stainless steel plate are its density of 8010 kg m^{-3} and Young's modulus $E = 195$ GPa.

The only remaining input to recreate the wave impact is the sloshing acceleration of the tank. An equation of the form Eq. 15 is fitted to the measured tank position. Note that only the position signal is used for the fit, but its second derivative still matches the measured accelerations, as shown in Fig. 3. The sloshing amplitude $a = 60.0$ mm is given constant for all tests.

$$x(t) = \begin{cases} c_0 + c_2t^2 + c_3t^3 + c_4t^4 + c_5t^5 + c_6t^6 & \text{if } 0 \le t \le t_r \\ -a\cos(\omega[t - t_\varphi]) & \text{else} \end{cases} \tag{15}$$

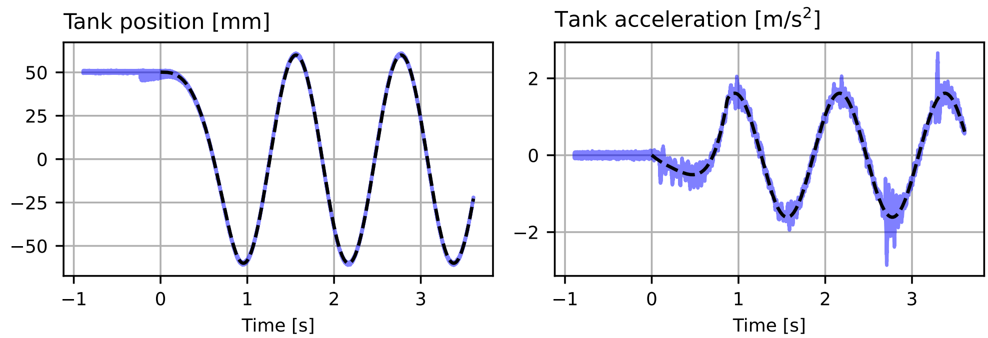

Figure 3: Example of motion fit for one test case ($\theta = 0°$, $d_t = 4.0$ mm, run no. 337).

Differences between repetitions of the same test case are small, so the mean of the coefficients is used to obtain a single fit for each test case. Coefficients $c_{4,5,6}$ are not averaged, but solved based on C^0 continuity of (x, $\dot{x}$, $\ddot{x}$) at $t = t_r$. The parameters required to reproduce the accelerations are given in Table 1.

For all simulations, the fluid domain of Fig. 2a is divided into square cells. The number of degrees of freedom are given in Table 2 for three refinement levels. The 1D structural domain is subdivided by placing FE nodes on vertical grid lines of the fluid domain. The subdivisions are chosen such that the same fluid domain can be used for both the horizontal and tilted plate. The tilted plate requires less cells for the same length, because it intersects fewer vertical grid lines. The two rightmost columns in Table 2 show the plate length as represented in the fluid domain resulting from these choices. Dynamic deflections are projected to the vertical grid lines corresponding to the initial state. When the beam is tilted, this projection causes a difference in the geometrical representation of the beam length in the fluid, which is accepted for the current implementation.

θ [deg.]	d_t [mm]	$a\omega^2$ [m s^{-2}]	t_φ [s]	t_r [s]	$2c_2$ [m s^{-2}]	$6c_3t_r$ [m s^{-2}]	$12c_4t_r^2$ [m s^{-2}]	$20c_5t_r^3$ [m s^{-2}]	$30c_6t_r^4$ [m s^{-2}]
0	4.0	1.6099	0.9538	0.8667	0.0331	-2.2801	5.5865	-10.6677	8.7772
0	0.4	1.6514	0.9599	0.8857	0.0426	-2.1469	4.3879	-8.3103	7.5546
30	4.0	1.6135	0.9539	0.8748	0.0018	-1.7344	3.0352	-6.4711	6.6482
30	0.4	1.6057	0.9533	0.8607	0.0718	-3.2192	10.1072	-17.8087	12.2741

Table 1: Sloshing acceleration parameters for considered test cases. Values are presented in a form that can be used directly in the second derivative $\ddot{x}(t)$ of Eq.15.

N_{F1}	N_{F2}	$\Delta x_{1,2}$ [mm]	N_F	N_{S0}	N_{S30}	Δs_{30} [mm]	$N_{S0}\Delta x_1$ [mm]	$N_{S30}\Delta s_{30}$ [mm]
175	140	3.331	24,500	30	26	3.847	99.94	100.02
350	280	1.666	98,000	60	52	1.923	”	”
700	560	0.833	392,000	120	104	0.962	”	”

Table 2: Degrees of freedom N_F and N_S for the fluid and structure domains, respectively. A distinguishment is made between the horizontal ($\cdot_0$) and tilted ($\cdot_{30}$) plates. Cell sizes are given for the fluid $\Delta x_{1,2}$ and the structure Δs_{30}. Note that $\Delta s_0 = \Delta x_1$.

4. Validation

The four test cases of Table 1 are reproduced numerically to validate the hydrostructural model for wave impact. In the results that follow, multiple physical test realisations are shown in the same figure using transparent blue curves to demonstrate the repeatability. Filtering is applied to the physical measurement signals by removing frequency components above 400 Hz using forward and inverse Fast Fourier Transform.

The plate deflection is shown only for the 0.4 mm plate in Fig. 4, because the 4.0 mm plate does not deform significantly compared to the laser precision. In the following text and figures, the 0.4 and 4.0 mm plates are also referred to as flexible and rigid, respectively. The comparison of deflection is interpreted mostly qualitatively, due to uncertainty in the exact position of the laser distance sensor in the physical measurement. The comparison shows similar temporal behaviour of the plate deflection in the measurements and the coupled simulation. The quasi-static deflection curves are discussed later in section 5.

Reaction forces are compared in Fig. 5, where a clear difference is the absence of oscillations in the simulations of the rigid plate. These force oscillations for the rigid plate are attributed to the elasticity of the load cell and is discussed further in section 5. Besides these oscillations, the reaction forces are of similar magnitude and temporal dynamics. The tilted, flexible case clearly shows large oscillations that can be attributed to the hydroelastic response of the plate itself. For the horizontal plate the magnitude of the peaks are similar, but the tilted plate experiences around two times higher peak forces in the simulation with the highest resolution.

Pressure measurements are compared in Fig. 6, where the values are relative to atmospheric pressure. For the horizontal plate, the magnitudes of measured and simulated pressure peaks are similar. The tilted plate, however, experiences around two times higher peak pressures in the simulation with the highest resolution. The lack of convergence of peaks values upon refinement on the tilted plate is thought to be related to the small relative wave impact angle, as shown in Fig. 2b.

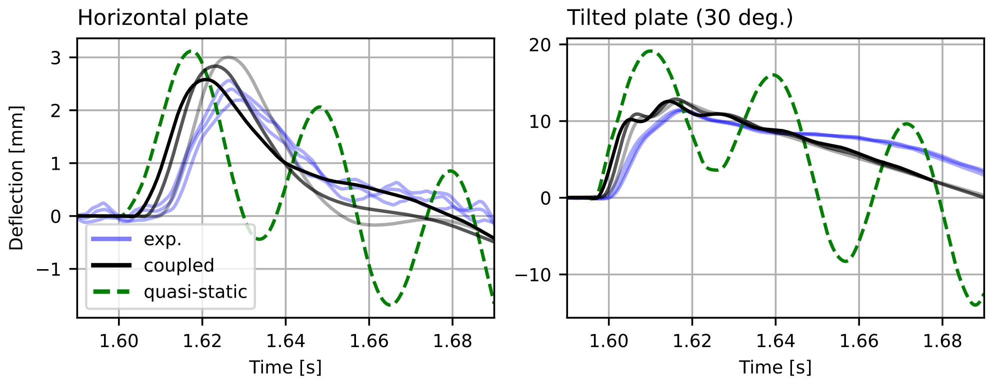

Figure 4: Comparison of measured and simulated deformation of the flexible 0.4 mm plate. Results for increasing grid resolution are shown with with decreasing transparency.

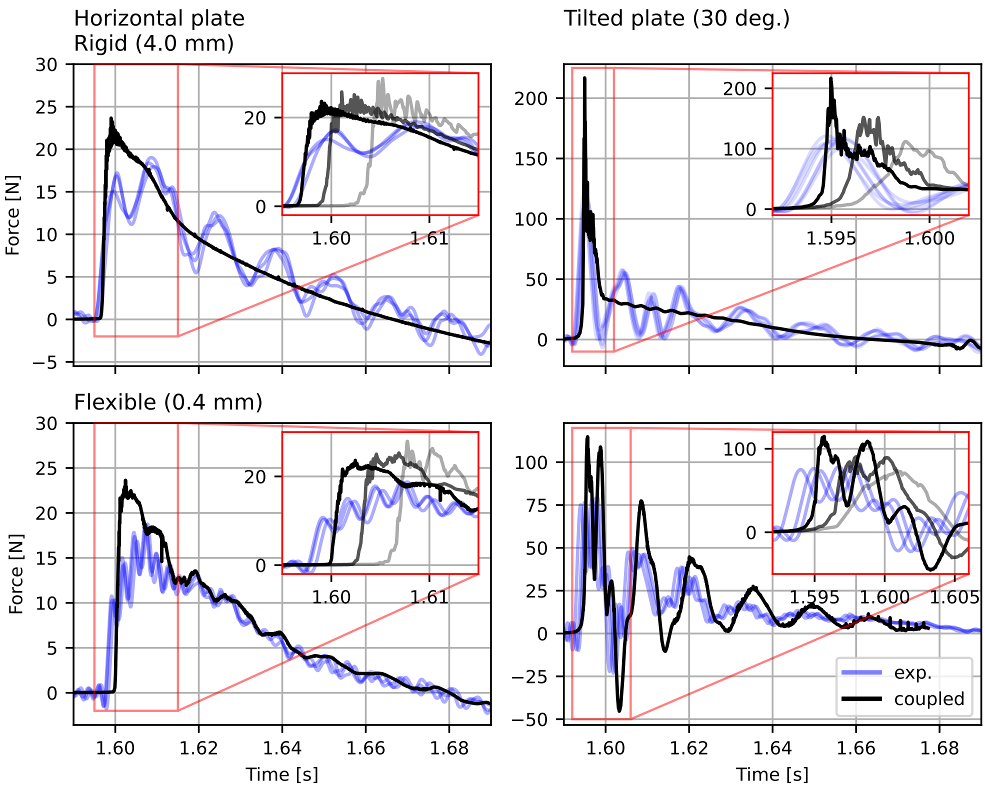

Figure 5: Measured and simulated reaction force. The insets show results for increasing grid resolution with decreasing transparency.

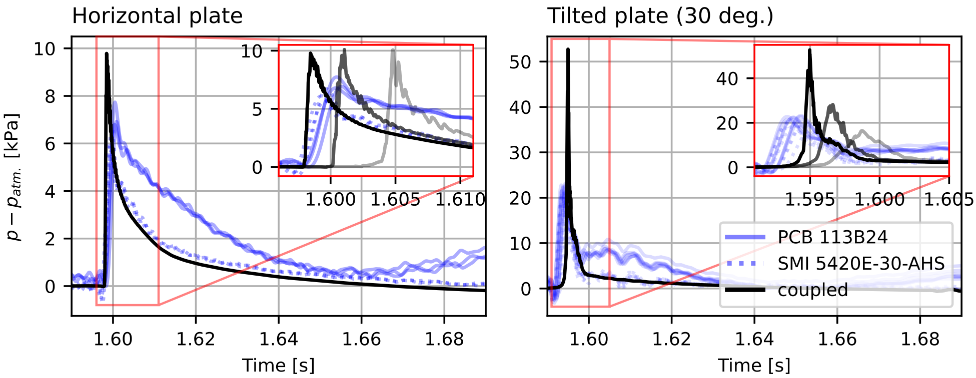

Figure 6: Measured and simulated pressure at a distance of 11 mm from the clamp. Two types of pressure sensors (PCB 113B24 and SMI 5240E-30-AHS) were used simultaneously at this length coordinate, placed at different locations in the third dimension. The insets show results for increasing grid resolution with decreasing transparency.

5. Hydroelasticity

In this section we discuss the observed effects of hydroelasticity in the wave impact experiment of the previous section. The elasticity of the reaction load cell is first discussed, followed by the effects of modelling plate elasticity on the total response.

5.1. Elasticity of the reaction load cell

The physical reaction force measurement for the rigid plate in Fig. 5 contains oscillations that can not be attributed to the plate deflection. These oscillations are absent in the numerical simulation of the same plate, which supports this statement. Instead, they are attributed to the excitation of a natural frequency of the measurement system originating from the combination of load cell stiffness and supporting clamp mass. For the lighter, flexible plate, the oscillations are of higher frequency due to its lower mass. The oscillations likely influence the response of the plate, making it difficult to separate the hydroelastic contributions of the support and plate bending. Steps to correct for the elasticity of the load cell, such as filtering out specific frequencies of the measurements, are not taken.

5.2. Elasticity of the plate

Two different numerical approaches for determining the structural response are compared. The first approach consists of two steps: Calculate hydrodynamic loads on a rigid plate and then apply these loads to a dynamic structural model of a thin plate. This approach does not take into account the hydroelastic interaction, so it is referred to as the quasi-static method. The second approach is the monolithically coupled hydroelastic model introduced in section 2, and is referred to as the coupled method.

The difference in deformation calculated with the quasi-static and coupled methods is visualised in Fig. 4. The maximum deflection of the horizontal plate is overestimated around 20 % by the quasi-static method compared to the coupled method. Additionally, without the modelling of the fluid-structure interaction, large oscillations in structural deformation remain after the initial excitation. These are not observed in the measurements or the coupled simulations.

The maximum deflection of the tilted plate is overestimated even more. This may be expected when looking at the duration of the impulse versus the first natural period of the plate, which is 31.3 ms according to analytical solution of Eq. 10. This natural period is also observed in the quasi-static oscillations after impact. The duration of the force peak on the rigid, tilted plate is clearly below 0.01 s, while the natural period is more than a factor 3 higher. Consistent with literature, this impact can be placed in the impulsive regime where dynamic, coupled response is reduced compared to the quasi-static estimate.

6. Conclusion

This work introduced a model for hydroelastic simulation of wave impact on thin plates. A physical reference experiment is used for model validation and instructions for its numerical reproduction are presented. The following conclusions are drawn based on the presented results.

The importance of accompanying physical experiments with suitable numerical ones is highlighted by the observations in the measured reaction forces. For the impacts on the rigid plate, the elasticity of the reaction load cell caused oscillations in its measured value, which were absent in the numerical simulations without a load cell. The numerical results are thus important for the correctness of and confidence in the interpretation of the physical measurements. For the most severe wave impact considered, the hydroelastic analysis resulted in significantly lower structural deformations compared to the quasi-static analysis, highlighting the importance of hydroelasticity from a structural perspective.

The lack of numerical convergence for small relative wave impact angles requires further investigation, such as the inclusion of additional physics in the model.

Acknowledgments

The authors thank Jimme Bromlewe for his work on the physical experiment referred to in this study.

References

[1] G. K. Kapsenberg. Slamming of ships: where are we now? *Philosophical Transactions of the Royal Society A: Mathematical, Physical and Engineering Sciences*, 369(1947):2892–2919, 07 2011.

[2] S. Malenica, L. Diebold, S. Hong Kwon, and D. Cho. Sloshing assessment of the lng floating units with membrane type containment system where we are? *Marine Structures*, 56:99–116, 2017.

[3] B. Buchner. *Green water on ship-type offshore structures*. PhD thesis, Delft University of Technology, 2002.

[4] S. van Essen and H. Seyffert. Finding dangerous waves—review of methods to obtain wave impact design loads for marine structures. *Journal of Offshore Mechanics and Arctic Engineering*, 145(6):060801, 03 2023.

[5] A. D. Boon and P. R. Wellens. Probability and distribution of green water events and pressures. *Ocean Engineering*, 264:112429, 2022.

[6] S. Tavakoli, M. Singh, S. Hosseinzadeh, Z. Hu, Y. Shao, S. Wang, L. Huang, A. Grammatikopoulos, Y. Pearl Li, D. Khojasteh, J. Liu, A. Dolatshah, H. Cheng, and S. Hirdaris. A review of flexible fluid-structure interactions in the ocean: Progress, challenges, and future directions. *Ocean Engineering*, 342:122545, 2025.

[7] O. M. Faltinsen. Hydroelastic slamming. *Journal of Marine Science and Technology*, 5(2):49–65, 2000.

[8] A. Bereznitski. Slamming: The role of hydroelasticity. *International Shipbuilding Progress*, 48(4):333–351, 2001.

[9] F. Dias and J. M. Ghidaglia. Slamming: Recent progress in the evaluation of impact pressures. *Annual Review of Fluid Mechanics*, 50(Volume 50, 2018):243–273, 2018.

[10] M. van der Eijk and P. R. Wellens. An efficient pressure-based multiphase finite volume method for interaction between compressible aerated water and moving bodies. *Journal of Computational Physics*, 514:113167, 2024.

[11] B. P. Leonard, A. P. Lock, and M. K. MacVean. Conservative explicit unrestricted-time-step multidimensional constancy-preserving advection schemes. *Monthly weather review*, 124(11):2588–2606, 1996.

[12] B. Duz, M. J. A. Borsboom, A. E. P. Veldman, P. R. Wellens, and R. H. M. Huijsmans. Efficient and accurate plic-vof techniques for numerical simulations of free surface water waves. *Proceedings of the 9th International Conference on Computational Fluid Dynamics-ICCFD9, Istanbul, Turkey*, 2016.

[13] R. Scardovelli and S. Zaleski. Analytical relations connecting linear interfaces and volume fractions in rectangular grids. *Journal of Computational Physics*, 164(1):228–237, 2000.

[14] M. van der Eijk and P. R. Wellens. Two-phase free-surface flow interaction with moving bodies using a consistent, momentum preserving method. *Journal of Computational Physics*, 474:111796, 2023.